Proceedings of the ASME 2010 3rd Joint US-European Fluids Engineering Summer Meeting and 8th International Conference on Nanochannels, Microchannels, and Minichannels
FEDSM-ICNMM2010
August 1-5, 2010, Montreal, Canada

FEDSM-ICNMM2010-30141

CFD INVESTIGATION OF AIR-WATER TEST STAND FOR THREE-STREAM AIRBLAST REACTOR FEED INJECTOR

Wayne Strasser
Eastman Chemical Company
Kingsport, TN, USA

Duane Brooker
Eastman Chemical Company
Kingsport, TN, USA

Joshua Earley
Eastman Chemical Company
Kingsport, TN, USA

Paul Fanning
Eastman Chemical Company
Kingsport, TN, USA

ABSTRACT

A large-scale parametric air-water test stand (AWTS) study involving more than 40 evaluations was carried out for the purposes of three-stream airblast reactor feed injector optimization; a subset of seven air stream combinations is discussed here. The role of CFD as a supplement to, or a replacement for, air-water testing is of great industrial interest. To this end a set of CFD experiments was carried out to mimic the AWTS study. A compressible geometric reconstruction Volume of Fluid (VOF) method was used to simulate the three-stream interaction. Pressure responses, spray opening characteristics near the feed injector face, and spray distribution were primary measures for both the AWTS and CFD programs. It was found that, over the range of variables studied, there was a partial match between CFD and AWTS results; some measures matched quantitatively, others qualitatively, and some did neither. A self-exciting, pulsatile spray pattern was achieved in CFD and AWTS, and an interesting transition in spray bursting character occurred at moderate inner air flows. Overall, it is shown that the CFD method contained herein can be used to supplement, but not replace, air-water testing for said injector configuration.

INTRODUCTION

According to Lefebvre (1989) and Lienemann, Shrimpton, and Fernandes (2007), the earliest quantification of jet disintegration was carried out by Felix Savart in 1833. Since that time, the breakup and atomization of jets has been of direct importance to, and the subject of great experimental and computational focus within, the agricultural, chemical, food, fire protection, and energy-production industries. In many fuel applications, the concept of "pre-filming" has been utilized. The point with pre-filming is to begin the wave disruption process deep in the nozzle and then use an orifice to generate the final, atomized spray. Typically this is done by exposing the primary liquid stream to a higher velocity stream of air. The use of air makes this approach fall into the category of "air-assisted" nozzles. Within the air-assisted category lies a special group of designs that involve relatively large mass flows of gas called "airblast" nozzles. While the dividing line between air-assisted and airblast is not precise, airblast nozzles generally exist in high-pressure (high gas density) applications in which the gas momentum is large relative to the liquid. Combustion systems are limited in the amount of excess air they can inject to maintain air-fuel ratio, but because of high-pressure operation, one might classify them as airblast applications.

In the present work, an airblast nozzle (injector) is used to generate an atomized fuel stream for a large-scale reactor. Three streams are used: inner jet gas, outer annular gas, and an intermediate annular liquid stream. US patents 6755355, 6892654, 6284324, and 6033447 describe said injector. Not only do the physics of liquid sheet instability come into play, but the turbulent interactions with an inner and outer shear (gas-liquid interface) become important. Depending on various operating parameters and conditions, the air streams could harmonically excite or diffusively restrain the liquid sheet. Three-stream injectors might be advantageous for controlled droplet size and distribution relative to typical orifice nozzles or swirl injectors. Piecewise optimization of said feed injector is made difficult by the interplay of geometry and shear field. For example, changing the positioning of the various entrances of gas and liquid relative to one another not only changes the length of time the sheet is exposed to disturbances but also changes the shear field. In addition to the challenges associated

with understanding the profound physics, making changes to a production scale feed injector is expensive as millions of pounds of product per year are at stake.

Fuel Injector Verification

Testing of oil and solid fuel slurry nozzles in pressurized processes creates challenges in determining spray patternation, which has a large impact on reaction rates within commercial reactors. These nozzles are designed to finely atomize a large volume of liquid by impinging high pressure steam, air, and/or oxygen while forming a relatively narrow spray angle. The net result is the formation of a dense, opaque spray pattern that contains varying droplets and ligaments sizes. One serious issue that arises with fuel nozzle testing is scale-up. Most new process designs start with bench scale size equipment that tests less than 1 kg/hr, while a commercial unit can process 120,000 kg/hr. During scale-up, the critical film thickness might change by 50x. Finally, in designing a nozzle, the geometry of the fluid passages and chambers may vary to meet other process restrictions such as pressure drop or excessive erosion. Without knowing if these slight changes will result in unforeseen changes to the spray pattern, project risk may become high. Therefore, the individual involved in designing large scale fuel nozzles needs to have test methods available that can correlate design changes quickly and inexpensively. Air-water testing of nozzles has been a common method for characterizing a wide range of nozzles. Over the years, researchers have built on previous work to obtain a better understanding of the factors that influence each nozzle type (airblast, pre-filming, plain orifice, etc); however, apparent disagreements between studies exist and are often blamed on differences in nozzle geometry and poor understanding of wave break-up. Considering much of the development work has been conducted with single phase liquids at relatively low pressures, working at high pressure with two phase liquids such as oil-water, oil-steam, or solid fuel slurries, adds even more uncertainty.

Pre-filming or pre-mix atomizers are typically used for atomizing fuel streams. These nozzles operate at high velocity to push the reaction front away from the nozzle's face. Lefebvre (1989) proposed generalized Equation 1 for a pre-filming, airblast atomizer.

$$\frac{SMD}{L_c} = \left[\begin{array}{l} A'\left(\frac{\sigma}{\rho_G U_G^2 D_p}\right)^{C'}\left(\frac{1}{\beta}\right)^{0.1} \\ + B'\left(\frac{\mu_L^2}{\sigma \rho_L D_p}\right)^{0.5} \end{array} \right] \left(1+\frac{1}{GLR}\right) \qquad \textbf{(1)}$$

Equation 1 implies, directly, that larger injectors produce larger droplets, but this is not a widely accepted certainty. The inclusion of Oh implies that aerodynamic forces are important and primary atomization is not enough to adequately describe the droplet production process. Other correlations are given in tabulated form, along with the major effects of variables on droplet size, in chapter 6 of Lefebvre (1989). For a specific nozzle design, the constants and coefficients must be derived from testing. The testing is accomplished by placing a nozzle in a pressurized test chamber and then measuring the SMD while varying the gas density (e.g. helium, air, argon) and the fluid flows (e.g. water, corn syrup, glycol). The L_c, or characteristic length of the nozzle, can be interpreted as the retraction distance of a tip, but it can also be taken as another dimension or retraction.

Unfortunately, testing large nozzles in these rigs becomes impractical when liquid fuel flows may reach 1600 liters per minute. Also, the equation (fitted constants in Equation 1) derived from the test rig is difficult to linearly scale up to a large commercial nozzle because scale-up may be based on interior residence time which isn't linear. In addition, liquid and gas characteristics vary depending on process design. During scale-up, a break point often occurs in which the original equation simply falls apart. Therefore, the most cost effective method for proving a large scale nozzle is: i) establish the basic equation for the nozzle using several small scale tests, ii) test the air-water ratio on the small pressurized rigs to assure the ratio yields constant results, and iii) use atmospheric air-water rigs in which large volumes of fluids can be sprayed into a collection tank and the spray pattern monitored by high speed cameras and collection tubes.

Taking a high pressure process and simulating it under atmospheric conditions has several drawbacks in itself. First, in order to measure the spray, it is easier to remove the spray from the confined space. The nozzle could be placed into an enclosure, but this will lead to measurement issues. Using Doppler radar or lasers might be applicable, but are still fallible and have a high cost. Back recirculation and thrust impact on droplet formations are therefore ignored during non-confined testing. Secondly, high pressure steam and fuel when converted to atmospheric conditions will provide either a different gas to liquid ratio (GLR), or a different differential velocity between the liquid and the gas. Often unrealistic flow rates will be generated going from high process pressures to low pressure air-water testing if the GLR is held to the actual process conditions. If the injector design is changed to keep the GLR constant as well as the velocity profile, the injector geometry is no longer meaningful. Ultimately, the GLR is selected based on matching several other parameters. The chosen GLR must be tested in a pressurized test rig to help assure an alternate reality is not established by the conflicting GLRs.

In-house test results have demonstrated that the above approach is valid under many cases. Similar pressure pulses have been measured during large and small scale injector testing which also correlated to pressure pulses in the

commercial unit. Spray angles and particle impact locations also correlate reasonably well with commercial data. This suggests that large scale test rigs (despite differences in fluid properties) can be used to screen large patternation changes using high speed cameras and collection tubes. For instance, a hollowed, 34° angled spray cone can be observed versus a dense center 32° angled spray cone with ligaments using these relatively inexpensive tools. Unfortunately, measuring actual droplet sizes in these sprays is difficult. For instance, atomization on the outside of the spray may be excellent, but rather large ligaments may be forming in the interior of the spray that are masked by the fine exterior droplets. Also, because the fluid properties are different between the AWTS and commercial process, ligaments that may break up during the air-water testing may not break up in the pressurized reactor, or vice versa. Strobe photography has been used in the past to help with characteristics, but this technique is expensive and time consuming.

Based on experience, AWTS methods have proven very useful in reactor nozzle design, and oil/fuel slurry injectors both in scale up, and changes to the nozzle design or process flows. However, the testing is still time consuming, expensive, and requires large pumps and compressors to supply the high flows. If the results from AWTS could be duplicated by CFD modeling, then a Design of Experiment (DOE) could be set up much faster to modify the different atomizer parameters. Based on the CFD selection results, the new atomizer can be tested to assure the impact on the commercial unit is not negative.

Previous Work

Theoretical

A thorough study of the development of radially thinning liquid sheets in quiescent air is given by Lienemann et al. (2007). As We increases, Kelvin-Helmholtz (KH) instability (driven by shear) was shown to disturb the balance between momentum and surface forces and cause sheet flapping. Typical wave thicknesses were above the theoretical inviscid thickness value. Wave propagation thins the sheets further. In addition, sheet perforations can be caused by entrained air and/or boundary layer (vorticity) development from the orifice and bulk orifice turbulence. These perforation events depend on the length and time scales of the turbulence structures. They study in-tact sheet radius and show a $L_C We^{-x}$ effect, where "x" ranges from 0.33 to 0.42. A dependence on phase density ratio, β, raised to a similar negative fractional power is displayed. Thinner sheets are obviously advantageous to fine droplets. Close to the rim of the sheet, waves change from a sinusoidal shape (linear instability) to a zigzag pattern (non-linear) as vortices are shed off wave crests and move into wave troughs. This is the onset of break-up. Their work outlines dominant wave frequencies and sheet thickness dependence on feed conditions and feed stream angles. They discuss how the local sheet Weβ value can produce a shift in the preferred mode of instability, with symmetric waves (in-phase) produced below 1 and dilatational (phase opposition) above 1. Symmetric modes grow faster. Lastly, they address azimuthal sheet curvature. When the inner sheet diameter is small compared to the outer, it behaves like a full jet. For large values, like that in the present work, it behaves like a thin, inviscid sheet, favoring linear stability analysis. Above a certain liquid viscosity, however, linear analysis could vastly over-predict droplet size. Things that reduce the mean droplet size also tend to narrow the size distribution of droplets (Lefebvre, 1989), including an increase in air velocity and/or a reduction in liquid feed rate.

Another study of atomization is given by Dumouchel (2008). He painstakingly outlines theories and findings related to cylindrical liquid jets, flat liquid sheets, air-assisted cylindrical jets, and air-assisted flat liquid sheets. His premise is that in order for a spray to form, there has to be initial disturbance(s) at the liquid-gas interface and a mechanism for those disturbances to grow. The final spray droplet sizes are individually set by a balance of local disturbances and local liquid cohesion force. For the air-assisted sheets, he found the details of the liquid flow to be of lesser importance than those of the surrounding gas. The important effects include total liquid momentum, gas vorticity, gas phase turbulence, and the recirculation zone outside of the nozzle.

Computational

A large body of work in the open literature involves modeling of spray nozzle internal and external flows. Most CFD studies involve an Eulerian-Lagrangian (E-L) description of the gas and liquid phases, followed by Eulerian-Eulerian (E-E) studies. Few involve E-E interfacial motion tracking, such as the volume of fluid (VOF) method. An even smaller set of airblast-related VOF studies apparently exists, as the authors could not find a single one. Due to the scarceness of VOF-based airblast studies, an attempt to glean information from many different types of works will be executed here. Arcoumanis and Gavaises (1998) studied orifice diesel injectors and found that hole cavitation enhances atomization and that the mechanical hole area is not an accurate representation of the true area available for flow. Ibrahim et al. (1998) used steady-state E-L for airblast gas-turbine injectors and found that an increasing cone angle lead to increasing spray dispersion. They found asymmetry in the distribution and proposed that a time-accurate solution would lead to improved understanding of temporal breakup. They propose that jet shedding frequencies may couple with combustor dynamics to cause combustion instability. An air-assist gasoline injector is considered by Chen, Wells, and Creehan (1998) who reviewed two different computational codes and two different droplet break-up models in an E-L framework. They found that a primary atomization model (balance of turbulence, inertial forces, and surface tension) was better for modeling a gasoline injector than a secondary atomization model (additional considerations of aerodynamic forces between droplet and surrounding air). In general, the premise is that the size of the smallest droplets is

comparable to the size of the coherent turbulent structures that are just large enough to overcome the surface energy when We is less than 10, which is well below that of the present work. They assume turbulence isotropy and the existence of an inertial subrange in the turbulence spectrum. Their primary atomization models took the common form in which the SMD is proportional to $L_C We^{-x}$ with modifications for a "real" radial turbulence kinetic energy (k) distribution, as opposed to a uniform value. They show SMD related to k^{-x}, which says droplet size increases as k decreases. The implication is that, ideally, primary atomization would occur in a region of high turbulence energy for a lower equilibrium droplet size. The concept of jet shedding tuning with combustion was further explored by Eckstein et al. (2003) who induced harmonic oscillations in the feed air stream using a siren. They found instantaneous SMD proportional to instantaneous $L_C We^{-x}$, where x ranged from 0.5 to 0.8 depending on whether air flow or temperature was the source of the We change. They also found that the overall spray geometry was not affected by the imposed forcing up to 850 Hz (amplitude unclear). Som and Aggarwal (2008) discuss evaporating and non-evaporating diesel sprays using a unique combination of ETAB (Enhanced Taylor Analogy Break-up) and CAB (Cascade Atomization and Drop Break-up) methods. They clearly outline modeling the joint growth of both KH and RT instabilities, as well as including the effects of droplet collision. They show that various E-L model parameters have a profound effect on the solution. Nozzle shape effects are not accounted for in that their formulation does not consider cavitation and continuous phase turbulence.

In general, E-L methods suffer from multiple limitations. First, they are limited to dilute dispersed phases, in that the dispersed phase is not accounted for in the continuous phase momentum equation. Secondly, an initial droplet size, shape, and spatial distribution must normally be assumed. Also, droplet interactions and wall collisions are difficult to model. Lastly, most E-L studies employ only 1-way coupling between the continuous and discrete phase, i.e. the continuous phase is allowed to add momentum or turbulence to the discrete phase, but not vice versa. Strasser (2008) discusses some feedback effects of the droplets onto the continuous phase for a liquid polymer spray. To avoid the E-L problem of an assumed starting particle field, a Linearized Instability Sheet Atomization (LISA) model was considered by Collazo et al. (2009) as part of a study of methanol combustion. The LISA model employs semi-empirical relations for film formation, sheet break-up, and atomization. Film thickness, disturbance growth, ligaments, and droplet production are methodically quantified. This method, in a steady-state sense, attempts to address the physics in the present work. They show modest agreement between experiments and computations in regards to radial SMD; general trends are correct. Computed droplet radial number density is a closer representation of the experiment than SMD.

There are a handful of spray-related studies that do not employ the E-L method. Steady-state isopropyl alcohol spray from a SIMPLEX atomizer, as well as a reacting diesel spray, is investigated by Founti, Katsourinis, and Kolaitis (2007) using both E-L and E-E CFD methods. Their E-E method involved a momentum solution for each phase, separately, with strong evaporation, but did not make any attempts to study phase interface development. The E-E method suffers from the lack of particle size distribution and mass loss effects, as well as being more time consuming to model. Despite these challenges, the E-E model predicts the experimental counterparts slightly better than the E-L method, especially for the reacting flows. Fu, Ishima, and Long (2009) used E-E, also without surface reconstruction, to study swirl flutes in pressure-swirl atomizers, and cavitation was found at the center and walls of the injection hole. An LES-VOF study of liquid hydrogen atomization from an orifice was carried out by Ishimoto et al. (2008). Here the compressive interface capturing scheme for arbitrary meshes (CICSAM) method from Ubbink (1999) is used to resolve the gas-liquid interface and a simple subgrid scale linear relation between dissipation and filter width is used to quantify turbulence scales. They cited evidence of Kelvin-Helmholtz instability at the interface forming liquid ligaments which stretched in a 3-D fashion to form droplets. They proposed that the initial surface disturbances were generated by internal nozzle turbulence, relaxation of the liquid velocity immediately outside the nozzle, and bulk recirculation in the modeled container. Since the small scale droplet formation and jet disintegration are determined by local gas-liquid velocity fluctuations (and surface tension, not mentioned), it is expected that turbulence model (and grid size, not mentioned) would be key players. This sentiment regarding the general importance of turbulence as the interface is echoed by Chen et al. (1998), as previously discussed, and Lefebvre (1989), who discussed resonance in the turbulence field playing a role in break-up when the small scale turbulence frequency matches the natural mode of an entrained droplet. Primary break-up of a turbulent liquid jet is treated with a joint level-set/VOF in a direct numerical simulation (DNS) by Menard, Tanguy, and Berlemont (2007). The authors give a precise picture of the development and application of their unique interface tracking method. They specifically address the implementation of the numerical methods and how they handle 3-D surface reconstruction in this very complex flow, along with the stencils needed to couple with DNS. A simple Rayleigh instability analysis is performed to validate the method. The extent of the liquid core was shown to be about 7 jet diameters, and ligament/droplet production along the length of the jet is shown in various stages.

In short, a study directly related to the present work has not been found in the open literature. The objective is to carry out an AWTS and a compressible VOF-based CFD study of an airblast atomizer. The presence of three streams in certain combinations produces an inherently unsteady, bursting flow field that requires careful statistical consideration. The effects of various stream flow combinations on the pressure response, flow field, and spray distribution are considered. More than 40 geometric and stream combination permutations have been

tested over the past year as part of the overall experimental program, but only 7 will be shown in depth here. This work is broken up as follows:

- METHOD
  - Air-Water Test Stand
  - CFD Model and Boundary Conditions
  - Numerics
  - Convergence and Time-Averaging

- RESULTS
  - Pulsatile Annular Liquid Sheet
  - Spray Pattern Metrics
  - Measurement Uncertainty
  - Transient Pressure Response and Flow Field
  - Water Collection Profiles (Spray Angle)
  - 3-D Versus 2-D Model Results
  - Conclusions
  - Future Work

NOMENCLATURE

a	Acoustic speed
A'-C'	Constants determine by nozzle design
A"-C"	Spray metrics
C	Constant pressure heat capacity
D	Molecular diffusivity
D_p	Pre-film diameter
E	Total energy
F	Surface tension body force
g	Gravity
GLR	Gas : Liquid ratio
h	Sensible enthalpy
k	Turbulence kinetic energy
L_c	Characteristic nozzle parameter
Oh	Ohnesorge number
p	Pressure
Pr	Liquid phase Prandtl number
SMD	Sauter mean diameter (D_{32})
t	Time
T	Static temperature
u	Velocity component
U	Velocity magnitude
We	Weber number

Greek

α	Phase designation
β	Liquid density: gas density ratio
ρ	Density
ε	Turbulence dissipation rate
ω	Specific dissipation rate
μ	Molecular viscosity
δ	Kronecker Delta
σ	Surface tension
ζ	Molecular thermal conductivity

Other Subscripts and Superscripts

L	Liquid
G	Gas
i,j,k,l	Tensor indices
t	Turbulent
‘	Fluctuating component

METHOD

Air-Water Test Stand

The piping containing the three streams is equipped with liquid-filled static pressure gauges and volumetric flow meters. The inner air stream has duplicate gauges near one another in the piping, and both air streams have multiple pressure taps along the feed networks. A median pressure is read from a gauge by taking the average of the visual maximum and visual minimum. Depending on the magnitude and frequency of the fluctuations, the visual median may be nothing like the actual pressure response arithmetic mean. Sizing of the lines and valves was based on preventing excessive pressure drop and flow distortions from forming that could cause unwanted pulsations in the lines. Valving and instrumentation was installed 10x diameters away from the nozzle. Large pumps and compressors supply up to several hundred gallons per minute of water and 500 ACFM of air. To help determine the spray angle, 41 vertical plexiglass tubes and floats were used to collect the spray droplets. The tubes are arranged linearly side-by-side, 20 to the right of center and 20 to the left of center, and therefore collect a single radial cut from the stream. The assumption is that the flow is uniform azimuthally, or is axi-symmetric. Other, more sophisticated means are available for water collection, such as those that are angled in toward the injector. The tops of the tubes were approximately 13 feet under the nozzle. A high speed camera was mounted to photograph the pattern frequency at the nozzle exit. The camera was set at 6000 FPS at 256x256 resolution. Computer programs were tested to measure angles, droplet size, and velocities. Lighting and vibration around the test rig created challenging conditions. Pulse distance, frequency and angle were determined by manual time-stamped video footage frame viewing and counting.

CFD Model and Boundary Conditions

A cross-section of the model layout is shown in Fig. 1. The three streams fed from the top are shown as outer air (OA), Liquid (L), and inner air (IA). All IA flow values throughout this work are disclosed as a value that has been normalized over the range of tested IA flows. The normalization method is as follows: (Relative IA flow of interest – Lowest tested relative IA flow) / (Highest tested relative IA flow – Lowest tested relative IA flow). In other words, all presented relative IA

flows are scaled from 0 (lowest tested) to 1.0 (highest tested). The injector inlets are much longer and torturous than what is shown and will affect the pressure transients discussed in an upcoming section. Known temperatures, flow rates, and properties for the AWTS are supplied at the inlets. Turbulence quantities were specified using typical rules, but these are not critical; the turbulence field will develop through the long inlets based on pressure gradient, boundary layer development, etc. The walls are treated as adiabatic and no-slip. All fluids leave the domain at the bottom, which is a pressure-outlet. The modeled geometry is actually 2-D axi-symmetric (2DA), but is shown as a full cross-section for the reader. This implies that the injector centerline is an axis. Other non-wall model boundaries are treated as "openings", at which flow can move into or out of the modeled domain. Of course a 2DA model is going to run tremendously faster than a full 3-D model. The significant disadvantage, however, is that any shed droplets are not accurately modeled as "droplets" per se. Since the geometry wraps uniformly in the azimuthal dimension, each droplet remains a uniform torus shape. In reality, sheet perforations (caused by velocity curl and turbulence as discussed in the open literature) and radial sheet thinning cause the ligaments to break up azimuthally. This limitation likely impacts the resulting spray distribution result from CFD relative to the AWTS.

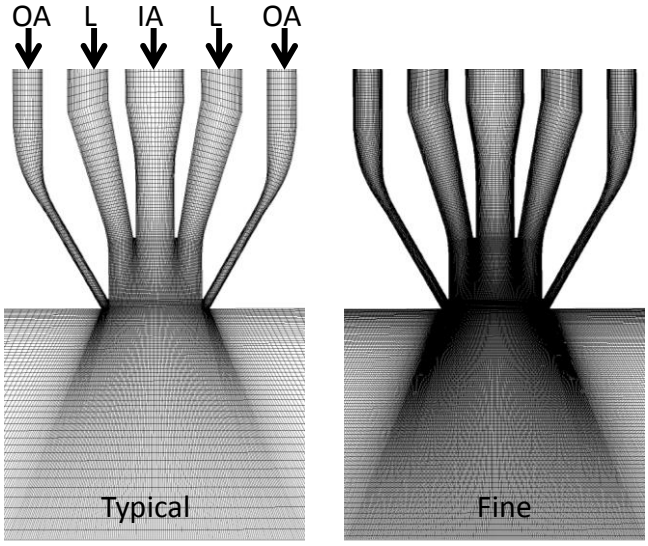

Fig.1: 2-D axi-symmetric CFD Model, typical and fine mesh, shown as a full cross section.

Two meshes are shown in Fig. 1, the typical mesh and fine mesh. The typical mesh contains about 32,000 elements per 2-D full cross-section, while the fine mesh is exactly 4 times that. To produce the finer mesh, all computational elements were simply cut in half in the radial and axial dimensions. Effects of mesh resolution will be discussed later and have been further explored in Strasser (2007). A 3-D model was run for one of the cases, and an end-section view of the mesh is shown in Fig. 2. Only 1/16th of the full circle (22.5°) was modeled with 20 cells. Notice the high aspect ratio (>100) cells at the bottom near the feed injector axis. Table 1 summarizes the various cases discussed in the present work. There are 7 flow combinations (FC) involving three overall air rates (undisclosed); however the total experimental program involved 41 tests over the past year. Water flow rate is held constant, while total air and IA are varied. It should be noted here that the present work includes a mesh evaluation for FC3, a solver evaluation for FC3, and a 2-D versus 3-D comparison for FC5.

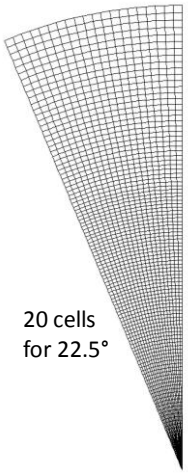

Fig.2: End view of a 3-D CFD model.

Table 1: Air flow combinations in the present work

FC Designation	Overall Rate	Normalized IA Flow
[-]	*[%]*	*[-]*
1	1	0.00
2	1	0.29
3	1	0.43
4	1	0.71
5	1	0.93
6	0.9	1.00
7	1.1	1.00

$$\frac{\partial \alpha \rho}{\partial t} + \frac{\partial \alpha \rho u_j}{\partial x_j} = 0 \qquad (2)$$

$$\frac{\partial \rho u_i}{\partial t} + \frac{\partial \rho u_i u_j}{\partial x_j} =$$
$$\frac{\partial}{\partial x_j}\left[\mu\left(\frac{\partial u_i}{\partial x_j} + \frac{\partial u_j}{\partial x_i} - \frac{2}{3}\delta_{ij}\frac{\partial u_k}{\partial x_k}\right) - \rho\left\langle u_i' u_j' \right\rangle\right] \quad \textbf{(3)}$$
$$-\frac{\partial p}{\partial x_i} + \left(\rho - \rho_{ref}\right)g_i + F_i$$

$$\frac{\partial \rho E}{\partial t} + \frac{\partial u_j\left(\rho E + p\right)}{\partial x_j} = \frac{\partial}{\partial x_j}\left[\begin{array}{l}\left(\zeta + \dfrac{\mu_t}{\mathrm{Pr}_t}\right)\dfrac{\partial T}{\partial x_j} + \\ \left[\mu\left(\dfrac{\partial u_i}{\partial x_j} + \dfrac{\partial u_j}{\partial x_i} - \dfrac{2}{3}\delta_{ij}\dfrac{\partial u_k}{\partial x_k}\right) - \rho\left\langle u_i' u_j' \right\rangle\right] u_j\end{array}\right] \quad \textbf{(4)}$$

Equation 2 reflects continuity, while equations 3 and 4 show the linear momentum balances and the energy balance, respectively, all in index summation notation. It can been seen that the gas and liquid share a common momentum and energy field, and properties are mass-averaged among the phase volume fractions present in a cell. With this method, film formation, ligament production, and droplet onset, as well as turbulence, are explicitly accounted for. The gradient diffusion hypothesis has been used to separate the molecular and turbulent diffusive effects in the conductive flux in equation 4. The air is assumed to behave as an ideal gas, and compressibility effects are modeled as shown in the deformation trace term in equation 3; the local Mach number can reach as high as 1.0 at any given time. Equation 4 provides that kinetic energy, viscous heating (including the total effective stress tensor), and pressure-work terms have been included in the analysis. Note that E is the total energy, which is simply $h-p/\rho+U^2/2$. Water droplet evaporation due to air humidity effects has been ignored.

The shear stress transport (SST) two-equation linear eddy viscosity model of Menter (1994) is used for computing the homogeneous turbulent contributions to momentum and energy transport. This model involves a smooth blend between the standard k-ε model of Launder and Spalding (1972) in the freestream and the k-ω model of Wilcox (1986) near the wall. In the SST model, additional consideration is given to the transport of the principal turbulent shear stress via 1) an eddy viscosity limiting function and 2) a cross diffusion term in the transport equation for ω. Also, there is a turbulence production limiter, as discussed in ANSYS (2009), preventing the artificial build-up of fluctuating velocity in regions of irrotational strain. "Scalable" wall functions, discussed in ANSYS (2009), are an alternative to standard wall functions of Launder and Spalding (1972). They have the advantage of being less sensitive to variation in near-wall grid resolution throughout the domain. The distance from the wall is computed via a Poisson equation with a uniform source value of -1. Additional compressibility effects have been included in the present work. That is, the typical constant known as "beta", which is used in the SST method (ANSYS, 2009) for the computation of the turbulent viscosity, production of turbulence kinetic energy, and the dissipation of turbulence kinetic energy, is adjusted for turbulent Mach number ($2k/a^2$) when turbulent Mach number exceeds 0.25. As with most Reynolds averaged turbulence models, the boundary layers are considered everywhere turbulent. It is well-known that eddy-viscosity turbulence computations are limited. The use of a fully differential Reynolds Stress model, and especially LES (many caveats, as discussed in Hanjalic, 2005) is too time-consuming for this "screening" stage in the project. Perhaps, since turbulence is 3-D by nature, employing a more advanced turbulence model might be warranted when modeling a 3-D domain. For the purposes of industrial feed injector optimization, it was decided that the use of a linear two-equation model was an adequate starting point.

Numerics

Equations 2 – 4 were solved in a segregated double precision ANSYS Fluent 12.1 commercial solver, with the exception of one test to compare 12.1 to version 6.3.26. The VOF method is a subset of the E-E mixture method and is one of the various options for seeking the definition of the gas-liquid interface (Menard et al., 2007). In the present work, the explicit "geometric reconstruction scheme" (Youngs, 1982) is used to solve equation 2 and assemble the interface in Fluent. A piecewise-linear function is assumed for the shape of the interface across each cell. According to ANSYS (2009), the geometric reconstruction scheme is the most accurate method of interface capturing currently implemented in ANSYS Fluent, more so than the CICSAM approach mentioned in the background section. Note, specifically, the downside to any VOF (or mixture) formulation; that is, phase equilibrium is assumed at the cell level. In other words, when droplets travel much faster than the surrounding gas, or vice versa, the slippage and shear layer generation between the two is ignored. This is a reasonable assumption for a fine grid in which there are multiple cells per droplet, but would not be the case in which there are multiple droplets per cell. The later is the case in any E-L framework. One would expect, therefore, the final solution depends on grid resolution. Pressure-velocity coupling is coordinated via the Pressure Implicit with the Splitting of Operators (PISO) scheme with skewness and neighbor corrections. A Green-Gauss node-based gradient method is used for discretizing derivatives and is more rigorous than a simple arithmetical grid cell center average. The pressure field is treated with a body-force weighted approach to help with body force numerics. Second-order upwinding is used for

advection terms, and first-order upwinding is used for the less certain turbulence quantities. QUICK would have been preferred, but was found to be unstable for this field. Details for the discretisation schemes can be found in Strasser (2007) and, most explicitly, in ANSYS (2009). The transient term is also discretized using first-order upwinding, but this is an ANSYS limitation. It can be noted, however, that with very small timesteps, this should not pose any numerical problems; each timestep represented only about $1/10{,}000^{th}$ of a normal spray pulsing event. Typical solver mass imbalances ranged from 0.001% (2-D) to 0.1% (3-D).

Convergence and Time-Averaging

The typical "iterative" (momentum and pressure solved at all inner loop steps) time-advancement technique is used to march forward in time at a timestep of 5.0×10^{-7} (2 million Hertz) with 10 inner loops required for residual flattening. Typical globally averaged Courant numbers remained below 0.5 throughout the runs. A normal 2DA run time can be from 1 to 4 weeks on 4 Woodcrest 5260 processor cores. The amount of run time necessary to characterize certain measures in a transient computational run is a critical matter. First, the results have to attain a quasi-periodic behavior in which the results are statistically stationary in time. Then, enough information has to be stored and averaged such that the average itself is stationary in time. Only the quasi-steady part and about another 0.1 seconds of flow time are required for pressure response and video analysis, but is not adequate for spray distribution measures. Water collection time-averaging (TA) took up to, and beyond, 1.0 second of run time. The 3-D model run time requirement was approximately 25 times that of its 2DA counterpart for a given TA requirement. This makes sense, given the fact that the 20 cells in the azimuthal direction consumes 20x of this time, while the other momentum equation and 3-D challenges consumes the rest.

Figs. 3 - 6 illustrate the necessity to run longer for certain measures. Fig. 3 shows one measure of TA time required. This is the arithmetic average (in time) of the maximum water volume fraction anywhere on the 3-D model outlet. It can be seen that it takes about 0.4 seconds of TA time for the 3-D model outlet values to stabilize. Fig. 4 shows a typical 2DA model measure, which is the total water collected within +/- 30% of the distance from the axis. This is similar to an AWTS water volume summation over +/- 6 tubes about the center tube discussed in an upcoming section. It stabilizes after about a second. It should also be noted here that the stabilization time somewhat depends on the data collection frequency. That has been optimized for the present work. Various stream flow configurations require different amounts of TA time. Figs. 5 and 6 clearly depict this for two different FCs. For FC3, the radial flow distribution is stabilized after 0.3 seconds, while FC6 requires greater than 0.65 seconds in order to equilibrate. More about the specifics of the spray pattern is to be discussed in a later section.

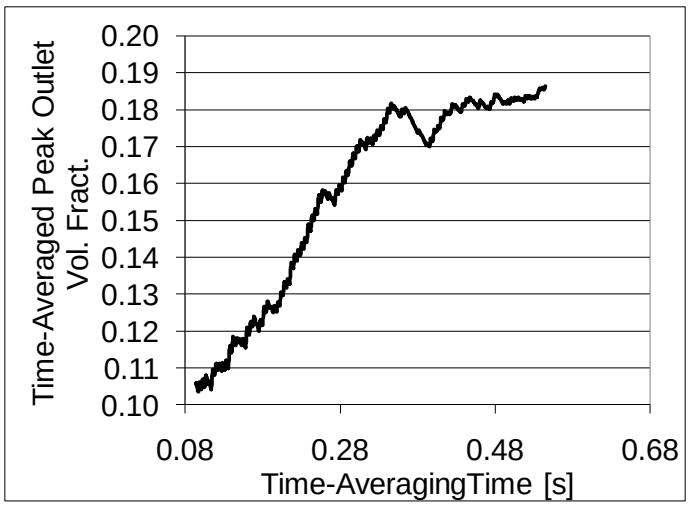

Fig. 3: Time-averaging time requirement for the 3-D model outlet time-averaged peak volume fraction.

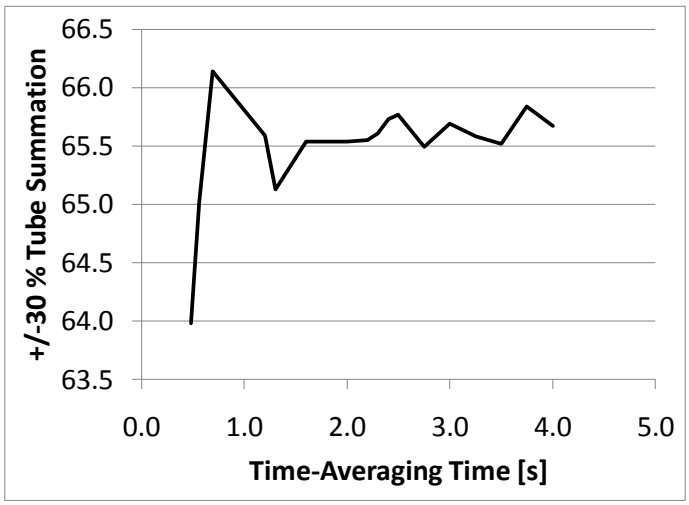

Fig. 4: Time-averaging time requirement for an important 2DA model water collection measure.

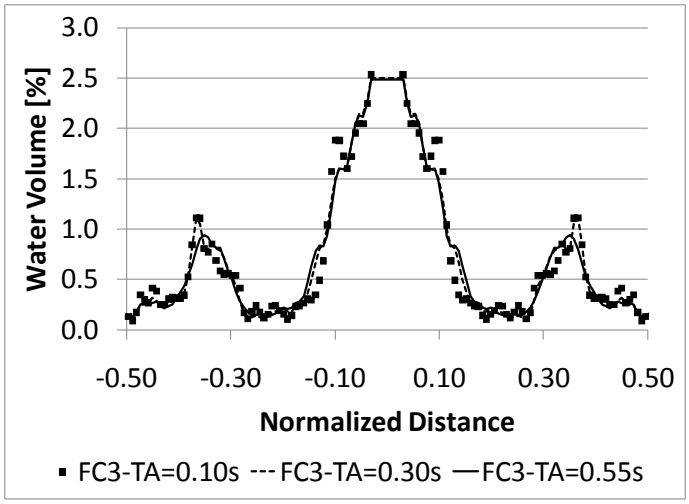

Fig. 5: Time-averaging time versus CFD spray profile from FC3.

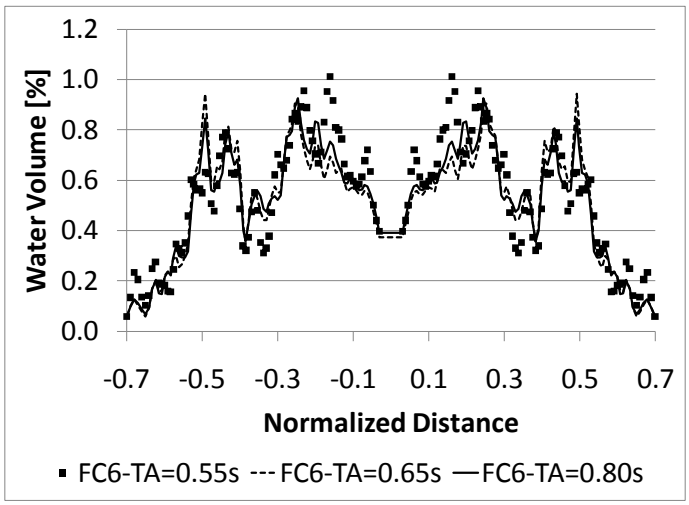

Fig. 6: Time-averaging time versus CFD spray profile from FC6.

RESULTS

Pulsatile Annular Liquid Sheet

Fig. 7 shows two CFD instantaneous contour plots of liquid volume fraction. Red represents liquid, and blue represents gas. The annular liquid film is excited by perturbations from both the inner and outer gas streams. Liquid can be seen peeling off outer and inner edges as well as bulk film fragmentation into ligaments (Dumouchel, 2008). There are at least 3 annular film driving frequencies in play here: i) shedding on the outside of the film layer from the OA (very fast), ii) shedding on the inside of the film layer from the IA (relatively slow), and iii) bulk flapping of the film layer (somewhere between the other two). Periodically, but not necessarily at regular intervals, the three frequencies tune together to produce five different types of pulsation events:

1. "Normal" bursts – The spray comes axially down away from the feed injector and then spreads normal to the feed injector face. The burst throws droplets radially outward. It can be seen in CFD and the AWTS video that this occurs at a frequency of about 200 Hz. A series of these can be observed occurring in the "Christmas tree" pattern in Figure 8.
2. "Half" bursts – For this event, the spray is only slung radially outward about half the radial distance of that of the normal burst. There are maybe three of these events occurring for every normal burst.
3. "Necking only" – Here, the stream radially narrows, but no outward bursting event occurs. There are approximately nine of these events for every normal burst.
4. "Blowback" – Approximately every 50 or so normal bursts is a blowback event, when the spray is thrown so violently outward that some of it actually moves axially in reverse and splashes back on the injector face. The strength and frequency of these events depends ***strongly*** on FC and feed injector geometry.
5. Inner gulps – This can only be observed in the CFD videos since the AWTS videos only allow the visualization from the outside of the spray. In this event, liquid bridges over the IA stream and is splashed back up into the IA inlet. The gulps occur at around 80 Hz.

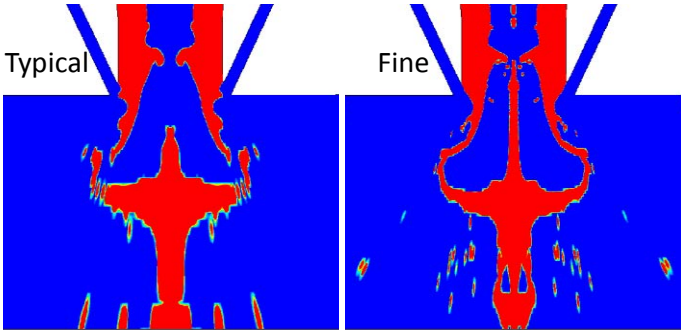

Fig. 7: General flow features showing the typical mesh (left) and fine mesh (right).

Two mesh-related issues can be noted from examining Fig. 7. The first is that the droplets are smaller and more prevalent with the finer mesh. Based on the fact that the VOF foundational assumption is that there are multiple cells per droplet, this makes perfect sense. The second is that the liquid inner bridges/gulps occur to a much larger extent in the finer mesh. In fact, the liquid only made its way back up passed the injector inlet plane with the fine mesh. As will be seen in upcoming discussions, however, a *major* mesh change only *partially* affected spray metrics.

The occurrence frequencies of the 5 events are, of course, a function of the various FC. From the AWTS and CFD video

observations, it can be seen that are three basic regimes of stream combinations that contain a finite amount of IA flow. One is "subcritical" in which the inner air stream is fairly easy to experimentally control from turning a manual valve and watching the corresponding flow meter. This occurs for low IA values, and only normal bursts can be seen here. Then, at intermediate IA flows, a "critical" regime is entered in which the air flow is very difficult to control. Pressure pulsations in the feed network are complex and erratic. All of the first 4 events can be seen in the AWTS videos of the critical flow regime. Lastly, at "supercritical" IA flows, the pressure pulsations in the feed network calm down again, but the AWTS video remains similar to that of the critical regime. Two other key flow regimes have been quantified in both the AWTS and CFD:

- If the inner air flow is removed, the bulk pulsation/bursting stops completely.
- If both air flows are removed, mild pressure pulsations are transmitted up through the water feed system, as the water flow, alone, produces a spray like that of any annular sheet in quiescent air.

Spray Pattern Metrics

The three spray pattern metrics for bursts are shown in Fig. 8. AWTS video snap shots are shown on top of CFD video snapshots. The only difference between the left and right is just that different dimensions are being highlighted. A" is the "neck width", B" is the "neck distance", and C" is the "shoulder distance". The neck width is measured at the thinnest neck of an event, at which point the neck distance off the injector face is also measured. The shoulder distance is measured from the injector face to the outer edge of the spray at the onset of another burst event. Of course, the AWTS videos show more droplets while CFD videos show more ligaments, so any metrics need to be comparable to one another from both video methods. It was for this purpose that these particular metrics focus on the continuous part of the annular liquid sheet. Manual frame-by-frame analysis is required to first find the event, and then to take said measurements. A series of multivariate analyses of variance (MANOVA) were carried out.

First, a solver comparison was made for FC3. Two solver versions, Fluent 6.3.26 and 12.1, were used for the same flow combination. The two simulations were started from the same prior quasi-steady results at a given timestep. The MANOVA revealed that for measures A" – C" there was not statistical difference between the two solvers' results; however, the 12.1 solver took notably longer to compute a given number of timesteps. The 12.1 solver was approximately 2.5x slower than the 6.3.26 solver given all equal settings. Then, a mesh comparison was made for FC3. The two meshes shown in Fig. 1 were run with the same conditions; however, each was allowed to reach quasi-steady state independently before data collection began. This starting point distinction will be important in upcoming figures. A statistical difference was detected between the two meshes for one of the measures considered. A" and B" were indistinguishable, but C" was about 18% larger for the finer mesh. In addition, all of the finer mesh measures had a higher standard deviation. These effects are consistent with the concept that a finer mesh provides a less diffused flow field; however, this difference is not enough to warrant a 4X longer computational time with such a encompassing experimental program. Perhaps a smaller increment of grid refinement can be evaluated to find an optimum point.

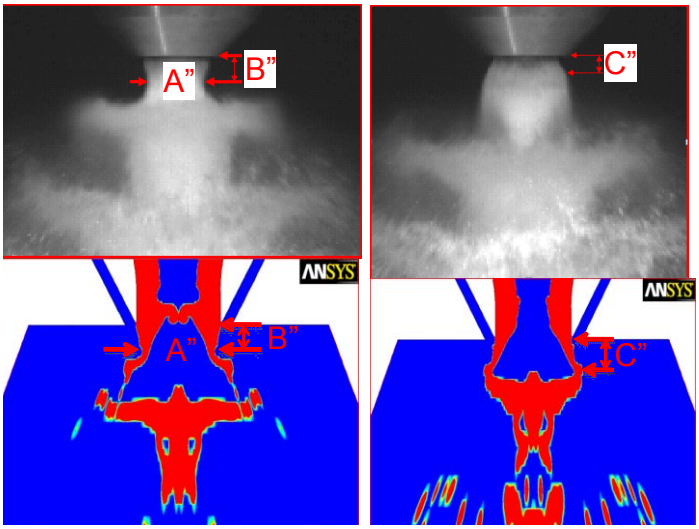

Fig. 8: Spray metrics showing AWTS snap shots (top) and CFD snapshots (bottom) for the purpose of illustrating the particular dimensions sought.

Then, each of the three measures was studied for a correlation between CFD and AWTS. It was found that A" and B" did not have a significant correlation between CFD and AWTS. The correlation coefficients for A" and B" were 0.03 and 0.4, respectively, and there was no detectable offset. The shoulder distance C", however, showed a significant correlation between CFD and AWTS. The coefficient was 0.7, and there was a statistically significant offset of 0.09 of the CFD result above the AWTS results. Lastly, each of the three measures was studied for functional dependence on IA based on the vast AWTS data set. The data were very scattered and too complex to look for linear relationships, but in general, the following trends were observed based on our data over the ranges tested:

- For measures A" and C", the value tends to be reduced by an increase in IA. This is counter-intuitive and says that the opening of the spray by increasing inner air tends to make *narrower* bursts *closer* to the feed injector face.
- For measure B", the value tends to increase with increasing IA. This is more intuitive and says that the opening of the spray by increasing inner air tends to make bursts occur *farther away* from the feed injector face.

Figs. 9 – 11 show the results in graphical form. There are 5 "sets" of data shown for each metric. Only the *population means* are shown at each point for each data set. In all cases, the units of the metric are purposely undisclosed.

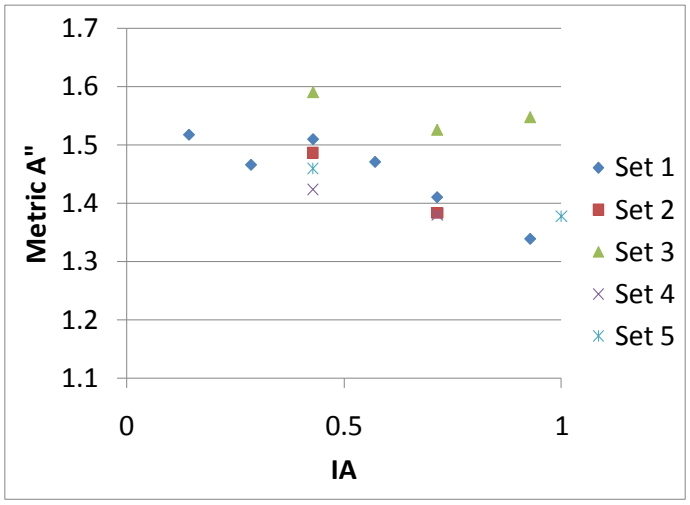

Fig. 9: Five AWTS data sets testing for IA functionality in metric A".

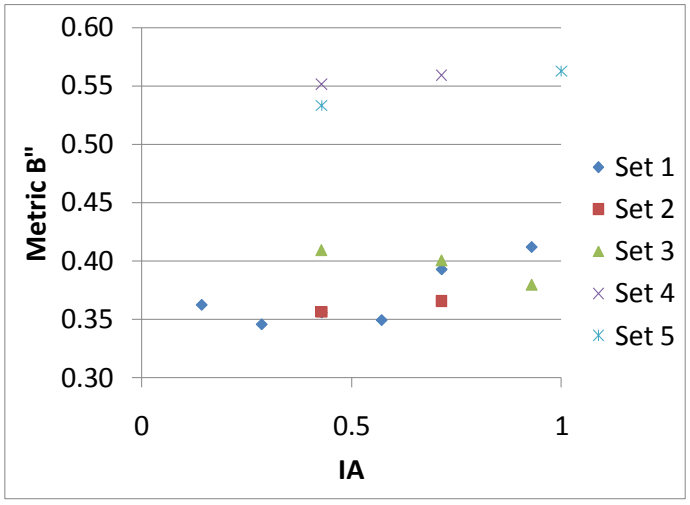

Fig. 10: Five AWTS data sets testing for IA functionality in metric B".

The question is, therefore, how both of these seemingly contradictory trends can be correct. They imply that the nature of the burst changes. As previously described, there are various types of bursts that are encountered as the relative IA is increased. By examining video footage of CFD and AWTS, the burst becomes more dramatic with increasing IA. The chosen metrics echo that response. As the IA increases, the neck gets narrower and farther from the feed injector face, while the outer shoulder gets closer to the face. The CFD C" results correlate with the AWTS C" metric, so this should be of great use moving forward in the program.

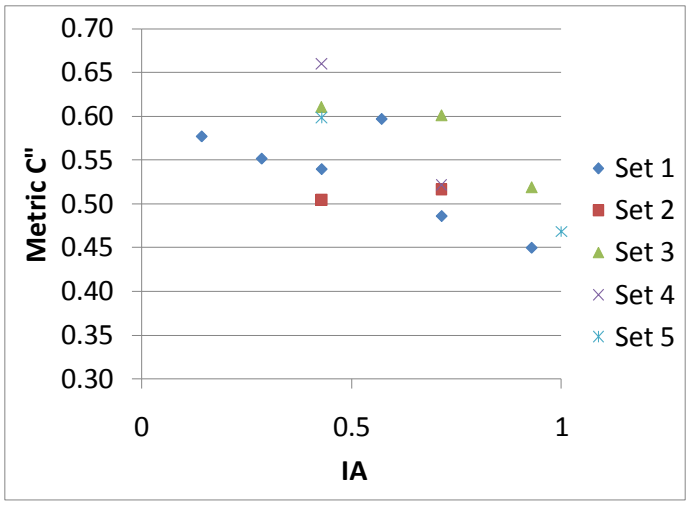

Fig. 11: Five AWTS data sets testing for IA functionality in metric C".

Measurement Uncertainty

The variability in the three metrics includes many sources. For the AWTS, these sources include air and water flow control, environmental conditions, limited length of the video collection time relative to the time scales of bursting events, and frame-by-frame video analysis issues. For CFD, the primary sources are those related to video analysis. Some of the data sets were repeated for both the AWTS and CFD in order to quantify the uncertainty. The standard deviation (n=9) for the three AWTS metrics ranged between 0.04 and 0.05 units, while that of the CFD results ranged from 0.05 units to 0.1 units. The largest CFD variability is for metric A", which also happens to involve the largest absolute value.

Transient Pressure Response and Flow Field

Pressure pulsations in the CFD inlets are shown in Figs. 12-15. The inner air (Fig. 12) responds at a frequency of about 200 Hz, which corresponds to the normal burst events. It can be seen that the response does not depend strongly on the computational mesh resolution. Data collection for the two mesh runs started at different run times (and zeroed out for the plot), so the realizations do not lie on top of one another.

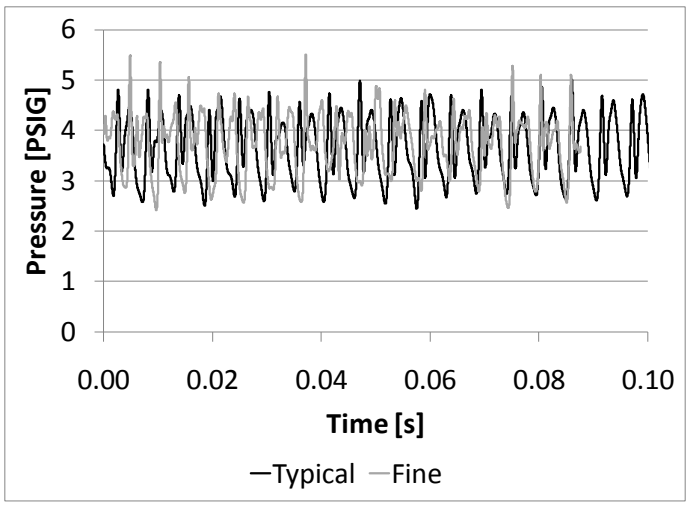

Fig. 12: FC3 pressure response for the inner air stream.

Fig. 13 shows pulsations for the same flow scenario but for the OA. Its frequency content is much richer, as it is likely dominated by the film outer edge shedding. The deviation about the mean is larger for the finer mesh by about 40%. This says that the typical mesh dampens out some of the oscillatory nature of the system. The means are indistinguishable.

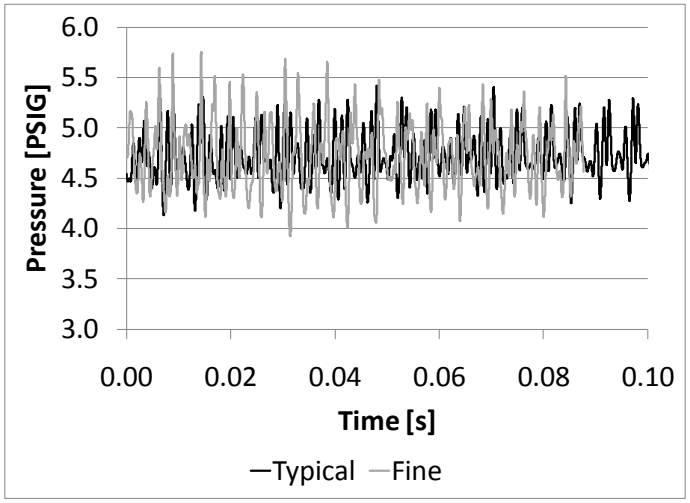

Fig. 13: FC3 pressure response for the outer air stream.

Fig. 14 shows IA pressure response in a comparison between Fluent solver 6.3.26 and 12.1. These runs involved the starting of the collection of data at the same time. Although this figure involves FC3, it is not expected that the pressure signal will be just like that of Fig. 12. For this run, an undisclosed geometry change makes these two runs different from the normal FC3 results discussed in the balance of this document. It is evident that the 12.1 flow realization is almost a duplicate of that of 6.3.

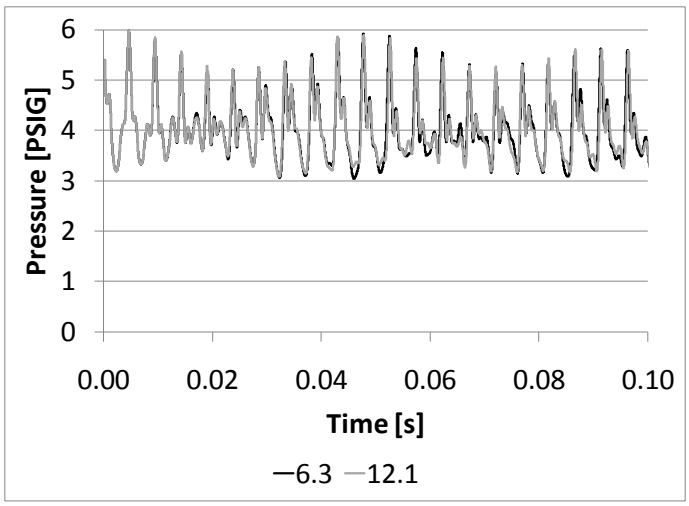

Fig. 14: FC3 (undisclosed geometry change from Fig. 9) pressure response for the inner air stream.

Fig. 15 shows the inner air pressure response for the five flow combinations at a constant rate. The higher IA tends to move at a repeatable, but not sinusoidal, 200 Hz. Overall, the fluctuation about the mean increases with IA. Notice, however, that FC4 is very different than the others. This implies that 0.71 is part of the regime shift between critical and supercritical.

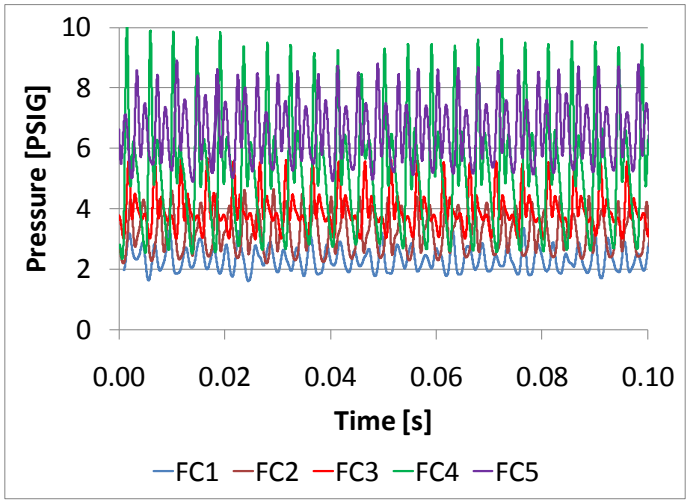

Fig. 15: Inner air stream pressure response for FC1-FC5.

The mean statistics for the inner and outer streams are shown in Fig. 16. The IA mean pressure increases in a squared response, as expected from Bernoulli. The IA deviation increases, in general, with increasing IA, but there is a clear peak at 0.71 as already noted. The OA mean and standard deviation do not depend on what the IA is doing. This implies that the outer air stream is somewhat isolated from the dynamics of the pre-filming section.

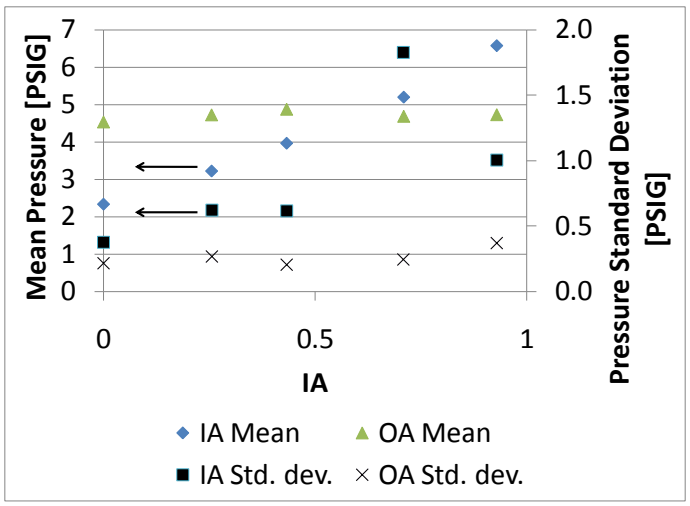

Fig. 16: Pressure statistics for all runs. The arrows indicate the referenced axis.

Although the median pressure from the analog pressure gauges on the AWTS is not computed the same ways as the true arithmetic mean from the transient pressure signal in CFD, it is useful to note that there is a general correlation between the two. (The AWTS method cannot detect the true max, min, or average.) The correlation coefficient for the OA feed stream mean CFD pressure and median AWTS pressure ranged from 0.75 - 0.91, while that of the IA feed stream mean pressure is only in the range 0.47 – 0.51, depending on the particular gauge considered. This difference makes sense given the noise in both streams, especially the IA stream. Based on Fig. 15, it is clear that these non-sinusoidal, asymmetric signals would be difficult to use to assign an "eyeball" pressure gauge mean.

It would be expected that the pressures are dampened at the inlets, which are undisclosed distances from the pre-filming region. Fig. 17 illustrates pressure contours for FC4. The scale is undisclosed, but blue represents low pressure, while red represents high pressure. Green represents the base, or outlet, pressure. Six generally sequential frames are shown throughout a burst event. These particular contour plots contain hundreds of timesteps between them, so it is not intended to be perfectly sequential. This visual sequence begins at # 1 with liquid bridging over the IA stream, building up back-pressure. The IA pressure continues to build into the next frame until it pushes through the center mass. Then, in the third frame, there is a contraction as the material leaves the pressure front. Next, the pressure starts to build again. In frame 5, it breaths again and neutralizes the IA inlet pressure signal. Lastly, the pressure is lowest in the pre-filming section, and the bimodal front is seen starting to develop. The OA pressure can be seen changing contour values as well.

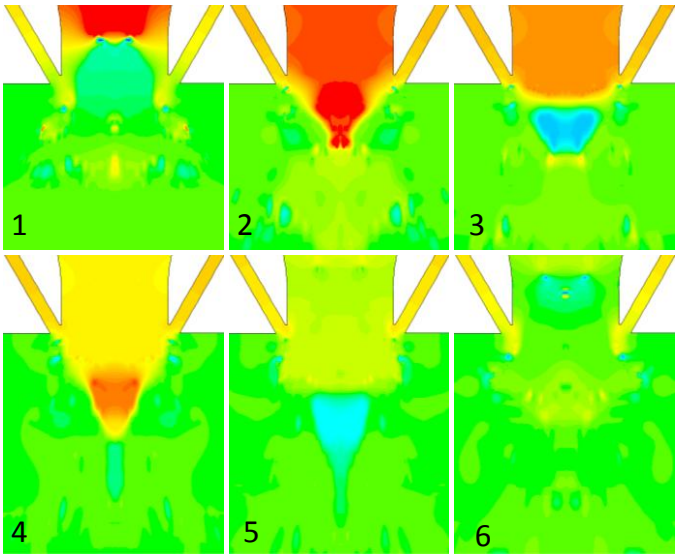

Fig. 17: Sample static pressure contour sequences for FC4. Many time-steps have occurred between frames.

To illustrate the velocity field that jointly works with the pressure field, Fig. 18 gives a sample set of instantaneous Mach number contours for FC5. Blue represents zero velocity, while red represents anything that has a Mach number of 1.0 or above. Locally speaking, the gas phase can easily become supersonic, as the effective flow area for the gas is reduced enough. In other words, mean velocity measures based on volumetric flow and orifice geometric area may not be good measures for ligament break-up correlation approaches in this system.

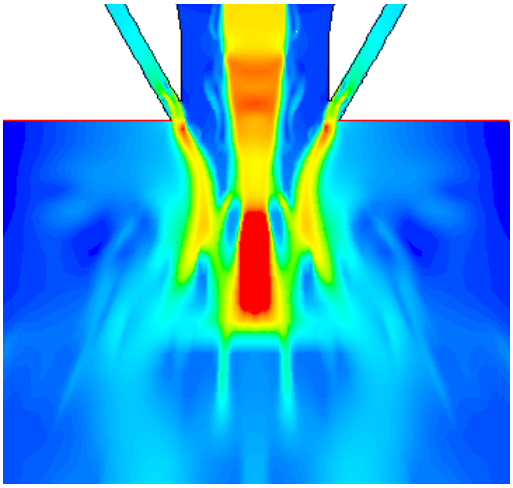

Fig. 18: Instantaneous Mach number contours for FC5. Blue = 0.0, while Red = 1.0 or above.

Yet another way to investigate the bulk flow field involves mean deformation. Fig. 19 shows two random instantaneous FC4 contours of the second principal mean deformation tensor

invariant as discussed in Strasser (2008). Blue is at or below an undisclosed negative number and represents areas of high strain rate. Red represents material at or above some positive threshold, i.e. areas of high vorticity. The frame on the left is just after a normal burst, while the frame on the right is just before a normal burst. In both cases, a rich field of alternating high strain/high vorticity can be seen at the phase interfaces. These areas, of course, produce and adjust the instantaneous turbulence field. A moving front of lateral vorticity/strain variation can be seen leaving the injector face just before the burst, but after the burst it takes on the shape of the moving phase interface.

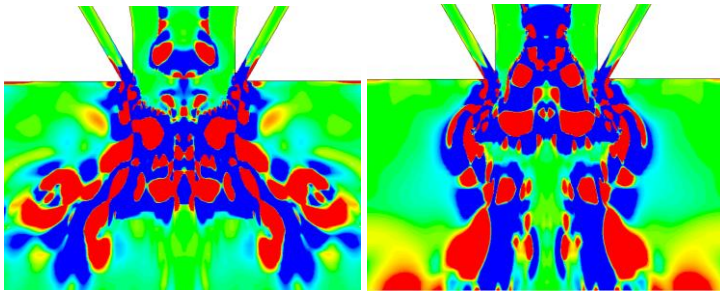

Fig. 19: Contours of second principal deformation tensor invariant at two random instants in time for FC4.

Water Collection Profiles (Spray Angle)

Water collection in the AWTS and CFD took place in an attempt to make directional comparisons in the effect of FC on spray angle. The project involved many more permutations than those shown here, and project duration was of immense importance. Due to the time requirement to gather sufficient time-averaged data, not all cases could be compared. In general, it is not fair to compare AWTS and CFD directly, because the AWTS collection system was 13 feet below the nozzle, contained 20 tubes to the left of center and 20 tubes to the right of center (41 total), and was sometimes affected by wind. The CFD "water collection" system, which involved time-averaging the water volume fraction on all the computational cells at the model outlet (Figs. 5 and 6, for example), was only 5" away from the modeled injector orifice. The purpose of the CFD outlet being so close to the injector was, of course, reduced simulation time. Fig. 20 shows the resulting AWTS water collection profiles for FC3, FC5, FC6, and FC7. The only difference between an "A" and "B" curve, where applicable, is that the data were taken at different times. Environmental conditions played a role in the results, although each "A" profile was reasonably close to its "B" counterpart. FC3 clearly has a unimodal distribution, FC5 has a trimodal distribution, and FC6 (high IA, low rate) has something between a bimodal and trimodal distribution; it is either a weak trimodal or an off-center bimodal. In any event, FC5 is almost indistinguishable from FC6. FC7 (high IA, high rate) seems to be leaning back towards unimodal, but remains trimodal with an extremely strong center peak. This is especially interesting, because it implies there is a strong interaction between overall rate and IA. If the profile is not shown here, it can be assumed that it was unimodal. Overall, this says that the IA has to be above the critical regime in order to produce a multimodal profile.

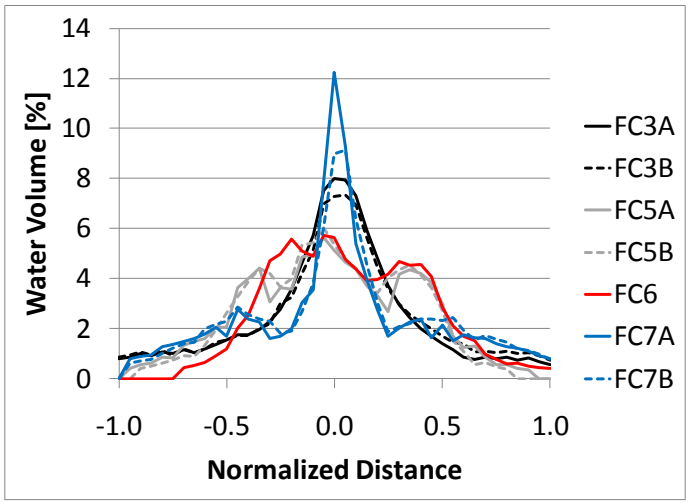

Fig. 20: AWTS water collection profiles for four flow combinations.

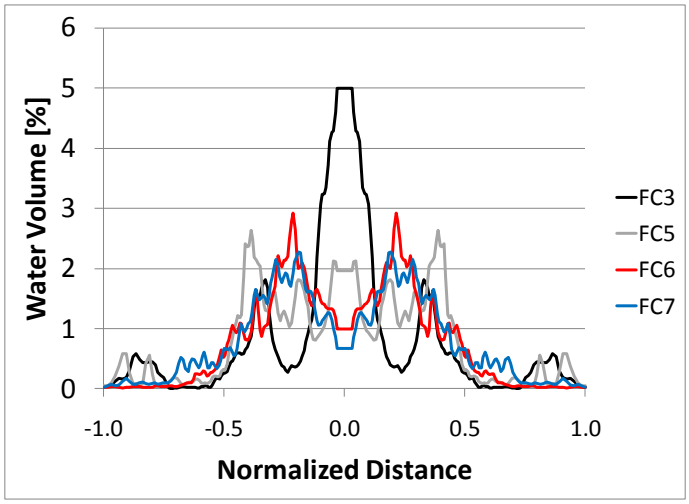

Fig. 21: CFD water collection profiles for four flow combinations.

The CFD results for FC3, 5, 6, and 7 are given in Fig. 21. Just like the AWTS profiles, the CFD profiles change dramatically above 0.71 IA. FC3 is center-peaked, while the others are not. FC5 is trimodal, while FC6 is narrower and bimodal; this is different from the AWTS result. The most striking difference between the Figs. 20 and 21 is the FC7 profile. The CFD FC7 result is more in line with the FC5 and FC6 results, while the AWTS FC7 is unique. Given the slight

difference between FC5, FC6, and FC7 conditions, and given the fact that all three are well above transition, the more questionable of the two curves is the AWTS profile. Again, the issue could be that CFD cannot capture the strong interaction between rate and IA. In all cases, the CFD results are noisier, as they contain more water collection resolution.

It is interesting to consider how AWTS angle measures correlate to those in CFD. As alluded to in Figs. 4-6, it takes longer for the +/- 6 tubes summation to stabilize than other measures. One measure that stabilizes sooner in CFD is the included angle that contains 50% by mass. One might consider using this to correlate with AWTS angle measures, but it only explains about 70% of the +/- 6 tube summation data. In addition, the low tube count on the AWTS makes a 50% angle difficult to calculate. It was found, therefore, that the +/- 6 tube summation should be sought as a quantifiable measure between AWTS and CFD. The correlation between the CFD measure and AWTS +/-6 tube water accumulation measure is shown in Fig. 22. This says that a linear relation between the two explains 60% of the variation, i.e. the CFD results track some of the AWTS data. If the lower rate run, FC6, is removed from the data set, the linear coefficient rises to 0.98. This issue coincides with the differences shown between Figs. 20 and 21. Either there is a very interesting effect of rate that CFD cannot pick up, or the experimental collection set is somehow wrong. As has been noted, there are a multitude of other statistical measures to describe spray angle; none of them on a comparative basis were significantly improved over that which has been shown here.

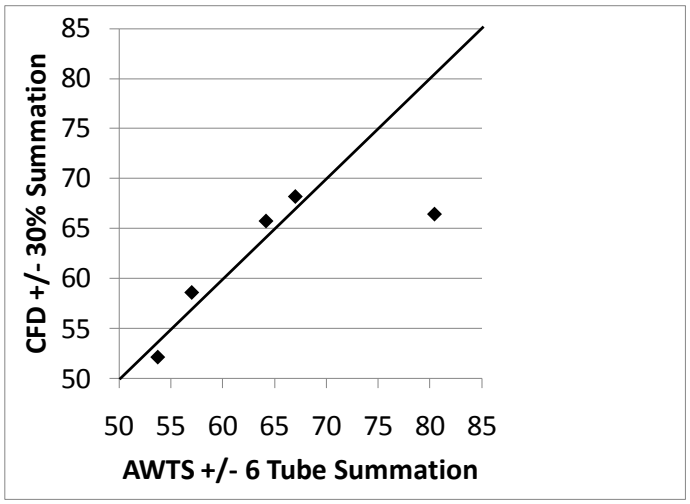

Fig. 22: CFD versus AWTS angle measure, which is the summation of all water in the tubes that are 6 spaces to the right and left of center. In CFD, this is equivalent to +/- 30% of the total distance across the outlet.

3-D Versus 2-D Model Results

Fig. 23 gives the said measure versus the relative amount of inner air for a constant total air rate in the AWTS data set. In general there is a decreasing trend, indicating a wider angle is being produced as the inner air is increased. This makes sense, considering the fact that the inner air would seem to provide part of the motive force for opening up the spray angle.

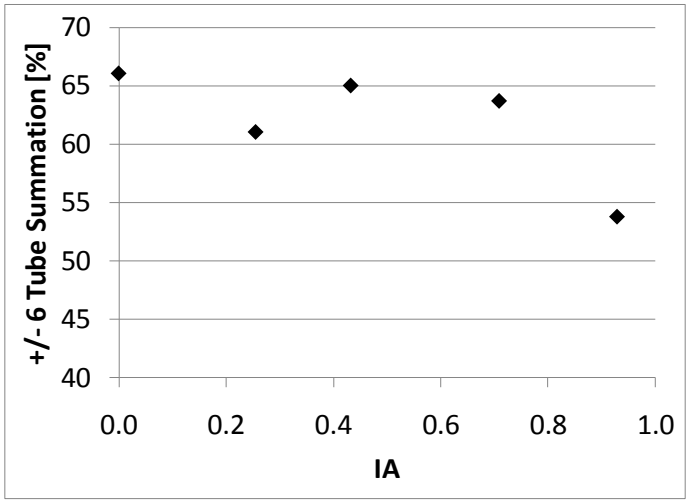

Fig. 23: AWTS angle measure, which is the summation of all water in the tubes that are 6 spaces to the right and left of center.

A 3-D CFD study was carried out on FC5 to compare with the 2-D axi-symmetric CFD results. It was found early on that said typical 2DA method would not converge in 3-D. The solver was repeatedly "tweaked", yet failed. A series of changes had to be made to the 3-D run to allow it to even work. The major changes included i) removal of the torturous inlets to reduce cell count, ii) treating the gas phase as incompressible, iii) changing the pressure discretisation to PRESTO!, iv) changing the momentum discretisation to QUICK, v) ignoring the gravitational field, vi) the use of single precision solver (since incompressible), vii) increasing the timestep by a factor of 10, and viii) doubling the inner loop count. Only changes ii) and viii) were for computational stability, while the other changes were for computational efficiency. The use of QUICK and PRESTO! for typical 2DA runs would also have been valuable (Strasser, 2010), but was found to be problematic when the compressible solver was used. The incompressible assumption allowed most of these changes and was the primary source of solution augmentation. These changes were also made to a 2-D run just for a comparative test with 3-D. The 2-DMM (modified method) case was 5x faster than the typical 2-D method. The speed-up came all from the time-step changes; the employment of PRESTO! and QUICK directly offset the use of a single precision incompressible solver. To review, the 3-DMM was approximately 25x slower than the 2-DMM approach.

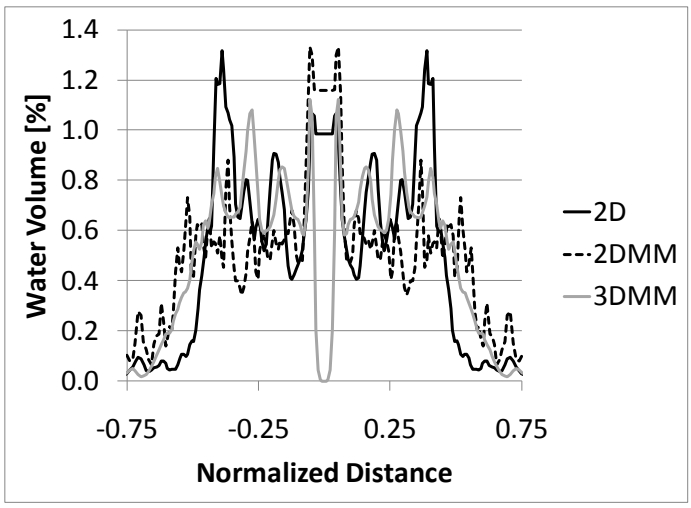

Fig. 24: CFD water collection profiles for FC5 exploring various methods and dimensions. "MM" indicates a modified solution method.

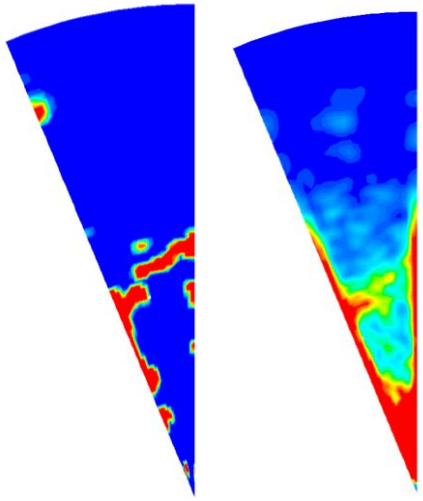

Fig. 25: Outlet water volume fraction contours (left is instantaneous, right is time-averaged) for 3-D run FC5. These results are problematic.

Fig. 24 shows the resulting water collection profiles from three runs: FC5 2-D (normal method), FC5 2-DMM (modified method to give a 1:1 3-D versus 2-D comparison), and FC5 3-DMM. It should be noted that the 2-DMM is not proposed to be the most accurate computational method; a fair comparison with the 3-D results was sought. A slightly less diffused spray pattern can be seen moving to the modified method in 2-D. This makes sense given the lack of gas phase "spring" (compressibility). The 3-DMM pattern looks similar to both patterns. The profiles follow a similar trend, but the center water concentration falls to nearly zero, like that of a purely hollow cone nozzle. In the spirit of further exploration, Fig. 25 shows an instantaneous water volume fraction plot and a time-averaged water volume fraction plot on the outlet for FC5. A few things can be surmised from this. First, the left and right side faces (symmetry planes) actually collect liquid, so 22.5° is not enough azimuthal modeling space. Second, there does not appear to be a discernable droplet size; there are rather larger blobs, i.e. the mesh is not fine enough for "droplets". Last, there is very little water at the injector axis, as is shown in the water collection profile in Fig. 24. The high aspect ratio centerline cells, seen in Fig. 2, might be responsible for erroneous interface reconstruction here. It is not evident whether the problem is related to the high-aspect ratio centerline cells or the general challenges with the 3-D VOF method discussed in Menard at al. (2007). Given the problematic water collection profile and the months of run time for this relatively coarse mesh on 4 modern processor cores, it can be concluded that this particular 3-D modeling prospect is not useful for the present undertaking.

Conclusions

An experimental and computational program has been executed to characterize the flow field produced by a three-stream airblast reactor injector at various stream flow combinations. More than 40 evaluations were included in the experimental program over the past year, but only 7 have been discussed here in detail. Compressible E-E geometric reconstruction VOF-based CFD models, requiring weeks of run time each, are statistically compared to AWTS pressures, spray angles, and spray shape metrics using MANOVA. It does not appear that any VOF-based airblast nozzle study has been documented in the open literature. Experimental uncertainty, along with tests of the CFD mesh count, solver version, and dimensionality reveal the useful conclusions below. In short, our CFD method (at this stage of development) cannot be used as a replacement for AWTS work, but it can be used to "screen" designs before spending the time and money to test them in the AWTS.

- Three distinct frequencies are at play to produce a liquid spray: shedding at the outer air/film interface, shedding at the inner air/film interface, and the bulk flapping of the annular liquid film.
- The tuning of these three driving frequencies produces five types of pulsation events: normal bursts, half bursts, necking only, blowback, and inner gulps. The existence and frequency of these events depend on the stream flow combinations.
- Depending on the relative amount of inner air flow, there seem to be three overall flow regimes. Low IA flows produce regular normal bursts. Moderate IA flows produce all five burst events along with violent AWTS feed piping network pulsations. Higher IA flows produce all five

events, but do not exhibit violent feed network pulsations. Somewhere near 0.71 IA flow appears to be the transition point, and it shows the largest fluctuations in IA feed pressures. Removing the IA completely causes bursts to stop all together. These are consistent between the AWTS and CFD.

- Water spray collection profiles from AWTS reveal that at low IA flows, the spray pattern is unimodal. At higher flows it becomes bi- or trimodal. There might be an interaction between IA flow and overall air delivery. The CFD spray pattern results track some of the AWTS flows directionally, while not others. Both sets of results show multimodal results above 0.71 IA flow.
- Three different video analysis "metrics" of the spray shape and burst quality were determined useful for quantifying the effect of inner air. They echo the fact that bursting becomes more dramatic with increasing inner air. CFD results correlate with one of the AWTS metrics.
- ANSYS Fluent versions 6.3.26 and 12.1 results are indistinguishable, while version 12.1 has a significantly lower (2.5x) computational progression rate given the same solver methodology.
- The typical mesh used for most of this work likely suffered some numerical diffusion, but a 4x refined mesh showed little to no change, depending on the measure.
- A 2-D axi-symmetric CFD model has proven useful for injector characterization; the 3-D model attempt did not provide much insight and was approximately 25x slower than its 2-D counterpart. It did not cover enough azimuthal extent and likely had cells near the injector axis with prohibitively high aspect ratio. If the azimuthal extent were doubled and more cell resolution added, the 3-D comparative slow-down will easily become >75x, making the problem prohibitively large for in-house computational clusters.

Future Work

The experimental program can be improved such that various measurement systems are used including; i) liquid nitrogen with sieves to freeze the droplets and classify the particles, ii) a Malvern particle analyzer to determine droplets in a fixed cross section, and iii) high speed strobe lighting to assist in recording pulsations, angles, and ligament distribution. Also, software for the automation of the frame-by-frame video analyses can be utilized, and this effort is currently underway. Lastly, the AWTS is being equipped with digital pressure transmitters. The computational program, of course, is far from perfect. A 3-D model with an improved near-axis mesh and wider azimuthal inclusion can be sought. If a useful 3-D model can be accomplished, it would make sense to try a more advanced turbulence model, such as a fully differential RSM. Isolating the effects on the reported results of discretisation schemes (and their associated under-relaxation factors) might be insightful. Also, the extension of the modeled domain to the length which matches the AWTS might be useful; it has been cost prohibitive thus far. Additional project plans include the evaluation of more geometric permutations as well as various combinations of individual stream swirling mechanisms.

ACKNOWLEDGMENTS

The author greatly appreciates the support of a multitude of Eastman Chemical Company personnel. Specifically, Glenn Shoaf, Molly Provost, Steve Hrivnak, and Dave Stevens were key contributors to this effort.

REFERENCES

ANSYS Solver documentation, 2009.

Arcoumanis, C. and Gavaises, M., 1998. Linking nozzle flow with spray characteristics in a diesel fuel injection system. Atomization and Sprays 8, 307-347.

Chen, J., Wells, M., and Creehan, J., 1998. Primary atomization and spray analysis of compound nozzle gasoline injectors. Journal of Engineering for Gas Turbines and Power 120, 237-234.

Dumouchel, C., 2008. On the experimental investigation on primary atomization of liquid streams. Exp Fluids 45, 371-422.

Eckstein, J., Freitag, E., Hirsch, C., Sattelmayer, T., Bank, R., and Schilling, T., 2003. Forced-low-frequency spray characteristics of a generic airblast swirl diffusion feed injector. Proc. ASME Turbo Expo.

Founti, M., Katsourinis, D., and Kolaitis, D., 2007. Turbulent sprays evaporating under "stabilized cool flame" conditions: assessment of two CFD approaches. Numerical Heat Transfer 52, 51-68.

Fu, L., Ishima, T., and Long, W., 2009. Simulation of the internal flow of the high-pressure swirl injector. Journal of Thermal Science and Technology 4, 294-304.

Hanjalic, K., 2005. Will RANS Survive LES? A View of Perspectives. J. Fluids Eng. 127, 831–839.

Ibrahim, M., Sanders, T., Yarwood, D., Moawed, M., Steinthorsson, E., and Benjamin, M., 1998. Spray characteristics of an airblast-simplex nozzle for liquid-fueled gas turbine combustors. Proc. International Gas Turbine & Aeroengine Congress & Exhibition.

Ishimoto, J., Ohira, K., Okabayashi, K., and Chitose, K., 2008. Integrated numerical prediction of atomization process of liquid hydrogen jet. Cryogenics 48, 238-247.

Launder, E. and Spalding, D, 1972. Mathematical Models of Turbulence. Academic Press.

Lefebvre, A., 1989. Atomization and Sprays. Hemisphere Publishing Corporation.

Lienemann, H., Shrimpton, J., and Fernandes, E., 2007. A study of the aerodynamic instability of attenuating liquid sheets. Exp. Fluids 42, 241-258

Menard, T., Tanguy, S., and Berlemont, A., 2007. Coupling level set/VOF/ghost fluid methods: Validation and application to 3D simulation of the primary break-up of a liquid jet. International Journal of Multiphase Flow 33, 510-524.

Menter, F., 1994. Two-equation eddy-viscosity turbulence models for engineering applications. AIAA-Journal 32(8), 1598 - 1605.

Som, S. and Aggarwal, S., 2008. A numerical investigation of non-evaporating and evaporating diesel sprays. Proc. ASME International Mechanical Engineering Congress and Exposition.

Strasser, W., 2007. CFD Investigation of Gear Pump Mixing Using Deforming/Agglomerating Mesh. Journal of Fluids Engineering 129, 476 – 484.

Strasser, W., 2008. Discrete particle study of turbulence coupling in a confined jet gas-liquid separator. Journal of Fluids Engineering 130, 1 –11.

Strasser, W., 2010. Cyclone-ejector coupling and optimisation. Progress in Computational Fluid Dynamics 10, 19-31.

Ubbink, O., 1999. A method of capturing sharp fluid interfaces on arbitrary meshes. Journal of Computational Physics 100, 26-50.

Wilcox, C., 1986. Multiscale model for turbulent flows. AIAA 24th Aerospace Sciences Meeting. American Institute of Aeronautics and Astronautics.

Youngs, L., 1982. Time-dependent multi-material flow with large fluid distortion. Numerical methods for fluid dynamics. K. W. Morton and M. J. Bianes (Eds.). Academic Press.

Youngs, L., 1982. Time-dependent multi-material flow with large fluid distortion. Numerical methods for fluid dynamics. K. W. Morton and M. J. Bianes (Eds.). Academic Press.